Flow (2023), **3** E21
doi:10.1017/flo.2023.14

FLOW CAMBRIDGE UNIVERSITY PRESS

RESEARCH ARTICLE

The influence of buoyancy upon pollution trapping and dispersal in the wake of a backward-facing step

Samuel Charlwood[1,*], Daria Frank[2] and Megan Davies Wykes[1,*]

[1]University of Cambridge Engineering Department, Trumpington Street, Cambridge CB2 1PZ, UK
[2]Department of Applied Mathematics and Theoretical Physics, University of Cambridge, Centre for Mathematical Sciences, Wilberforce Road, Cambridge CB3 0WA, UK
*Corresponding authors. E-mails: spc49@cam.ac.uk, msd38@cam.ac.uk

Received: 20 January 2023; **Revised:** 6 April 2023; **Accepted:** 21 May 2023

Keywords: Buoyancy; Pollution; Wakes; Wall plumes; Convection

Abstract

The importance of buoyancy relative to free-stream flow is described using an adapted Froude number $Fr' = U/f_0^{1/3}$, where U is the flow speed and f_0 is the exhaust buoyancy flux per unit length. We varied Fr' by changing the free-stream flow rate, the exhaust flow rate and the buoyancy of the exhaust. We have experimentally identified two flow regimes, depending on the value of Fr'. For high Fr' (low buoyancy), dispersion is driven by inertial forces in the wake and the amount of a pollutant in the wake is independent of Fr'. For moderate Fr', a wall plume develops up the back of the step, directly feeding the pollutant into the shear layer, but without altering the shape of the wake. This wall plume reduces the amount of pollutant trapped behind the step. We developed an analytic model to describe the quantity of pollutant trapped behind the step. The model predicts the transition from buoyancy being negligible to being the dominant transport mechanism within the wake. We have hypothesised and observed some evidence of a third regime at low Fr', when the buoyancy is sufficient to distort the macrostructure of the shear layer and wake.

Impact Statement

What effect does buoyancy have on pollution dispersion behind a backward-facing step? The answer to this question has wide-ranging applications, such as smoke trapped behind a burning building or dispersion of buoyant pollutants in wide street canyons.

With a growing global urban population, we are increasingly situated in close proximity to a multitude of sources of harmful airborne pollution with numerous documented health implications. Understanding and quantifying the mechanisms that transport these, often buoyant, pollutants can help to understand and reduce human exposure. At the low flow speeds associated with urban environments, the effects of buoyancy can be significant. We find here that the concentration of a pollutant trapped in the wake of a building is reduced if that pollutant is positively buoyant. We present a model to predict this reduction in concentration.

1. Introduction

The backwards-facing step is a canonical wake flow that appears in many scenarios ranging from street canyons to aspects of aerofoil design (Mishriky & Walsh, 2016). Here, we investigate the effect of buoyancy on pollution dispersion in the wake. Some examples of practical interest include trapping of

© The Author(s), 2023. Published by Cambridge University Press. This is an Open Access article, distributed under the terms of the Creative Commons Attribution licence (http://creativecommons.org/licenses/by/4.0/), which permits unrestricted re-use, distribution and reproduction, provided the original article is properly cited.

https://doi.org/10.1017/flo.2023.14 Published online by Cambridge University Press

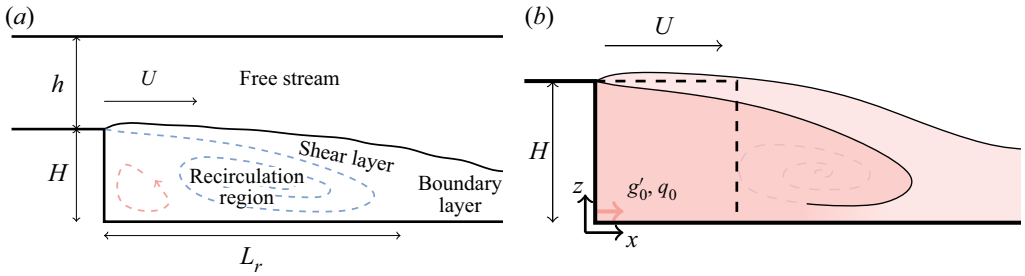

Figure 1. *The backward-facing step. (a) Flow structure. A shear layer forms where the flow separates at the top of the step, reattaching to the ground some distance L_r behind the step. After reattachment the wake structure feeds into a boundary layer. Two vortical structures form in the recirculation region: a larger primary vortex (blue) and a smaller secondary vortex (red). (b) Problem set-up. Step height H, free-stream flow speed U and a buoyancy flux per unit depth of $f_0 = g_0' q_0$, where g_0' and q_0 are the exhaust buoyancy and volume flux per unit depth. Dashed lines indicate an $H \times H$ box over which the concentration will be averaged, allowing comparison of theory with experiments.*

smoke behind a burning building and dispersal of pollution within street canyons (Simoens, Ayrault, & Wallace, 2007). The backward-facing step also represents a simple model to investigate the effect of buoyancy on wakes more generally, and as such could provide insights into vehicle pollutant dispersion.

The turbulent wake structure of the backward-facing step has several important features (figure 1*a*). As the free-stream flow passes over the step, a shear layer forms. The shear layer encompasses a recirculation region of low-speed flow located behind the step and eventually reattaches to the ground. Many studies, such as those by Adams and Johnston (1988) and Tihon, Pěnkavovà, Havlica, and Šimčik (2012), have investigated how L_r, the reattachment length, changes with Reynolds number ($Re_H = UH/\nu$) and expansion ratio ($E_r = (H + h)/h$; see figure 1*a*). As found by Nadge and Govardhan (2014), L_r increases with both E_r and Re_H, levelling off as the flow becomes Reynolds invariant, at a value of Re_H which depends on the value of E_r. The free-stream turbulence levels also affect the reattachment length, as does the thickness of the boundary layer when it separates over the step (Chen, Asai, Nonomura, Guannan, & Liu, 2018).

At sufficiently high Reynolds number, a separated recirculation region forms behind the step that contains two counter-rotating vortical structures (Chen et al., 2018). The primary recirculation (figure 1*a*, blue) is the larger of the two and is driven by the shear layer, with the top half of the primary recirculation forming part of the shear layer whilst the bottom half forms the lower bounding velocity for the shear layer. The smaller secondary recirculation (figure 1*a*, red) is located at the base of the wall of the step and driven by the primary recirculation region. Chen et al. (2018) provide a more extensive review of the flow structure behind the backward-facing step.

Significantly fewer papers have investigated the influence of buoyancy upon the wake of the backward-facing step. Existing research has focused on the case where the step is rotated at right angles to that shown in figure 1(*a*). A downstream 'floor' is uniformly heated and flow is in the vertical direction such that buoyancy either directly assists or opposes the wake (Abu-Mulaweh, Armaly, & Chen, 1993; Iwai, Nakabe, Suzuki, & Matsubara, 1999; Niemann & Fröhlich, 2016). This research has shown that when the buoyancy force aligns with the direction of flow, buoyancy reduces the wake size, while when buoyancy opposes the flow the wake size increases.

There has been some initial research into the effect of buoyancy released into the near wake of a floor-mounted cube (e.g. Lin, Ooka, Kikumoto, Sato, & Arai, 2020; Olvera, Choudhuri, & Li, 2008; Tominaga & Stathopoulos, 2018). Those authors have investigated the effect of pollutant source location and the effect of additional cubes up- and downstream. So far, this research has been largely qualitative, has not examined a wide range of buoyancy fluxes or explained the physical mechanisms behind the changes observed in pollution dispersion. Experiments performed within a wind tunnel by Olvera et al.

https://doi.org/10.1017/flo.2023.14 Published online by Cambridge University Press

(2008) found that increasing the buoyancy of the pollutant moves the concentration and velocity wake profiles upwards. This phenomenon was still significant at five cube heights downstream. Using an 'origin correction' method Robins and Apsley (2018) introduced buoyancy into their Gaussian plume model of pollution dispersion behind buildings; however, their model focuses upon far-field pollutant concentrations rather than the near field examined in this investigation.

We systematically examine the effect of buoyancy on pollutant dispersion directly behind the step, for a range of free-stream flow speeds, exhaust buoyancies and exhaust fluxes and develop a model that describes the observations. We outline the problem in § 2 and present some dimensional reasoning, alongside a model that predicts the total pollutant concentration trapped in an $H \times H$ region behind the step. Section 3 outlines the experimental methods, while § 4 details and discusses the experimental results. We demonstrate that increasing the buoyancy of the pollutant behind the step or decreasing the flow velocity leads to a reduction in the average concentration trapped there. We conclude in § 5.

2. Problem outline and theory

In this section, we outline the problem and the relevant non-dimensional parameters. The relevant variables are illustrated in figure 1(*b*). There are six dimensional parameters in the problem that can be controlled independently: the free-stream velocity U, the step height H, the viscosity of the working fluid ν, the exhaust concentration volume flux $c_0 q_0$ and the exhaust volumetric as well as buoyancy flux per unit depth, q_0 and $f_0 = q_0 g_0'$, respectively. Thereby, $g_0' = g(\rho_0 - \rho)/\rho$ is the reduced gravity of the exhaust, g is the gravitational constant, ρ_0 and ρ are the densities of the exhaust and the free stream, respectively, and c_0 is the concentration of the exhaust.

The units in the problem are time, length and a measure unit for the pollutant concentration. We choose the free-stream velocity U, the step height H as well as the concentration volume flux per unit depth $c_0 q_0$ as the repeating variables. The remaining three dimensional parameters can be non-dimensionalised and we form three dimensionless groups: the step Reynolds number, an adapted densimetric Froude number and a dimensionless flow rate analogous to an exhaust dilution rate:

$$Re_H = \frac{UH}{\nu}, \quad Fr' = \frac{U}{f_0^{1/3}}, \quad \hat{q}_0 = \frac{q_0}{UH}. \tag{2.1a–c}$$

As found by Armaly, Durst, Pereira, and Schönung (1983) and others, at a high enough Reynolds number, the flow around the step becomes Reynolds invariant, which is discussed further in § 3. Furthermore, our experiments have been designed such that $\hat{q}_0$ is small. This is outlined in more detail in Appendix B.2 and discussed further in § 4. Performing our experiments in the Reynolds-invariant regime, and considering $\hat{q}_0 \approx 0$, allows the collected experimental results to be scaled purely in relation to the adapted Froude number Fr'. The upstream flow has been laminarised using two layers of flow-aligning mesh and foam, and as such the turbulence generated within the wake is considered to be much larger than that of the free-stream flow. Hence, the results presented may not be directly applicable to scenarios with considerably turbulent free-stream flows. Caton, Britter, and Dalziel (2003) investigated and modelled dispersion mechanisms in a street canyon for high and low levels of external turbulence. Furthermore, the scenario is considered to have a small boundary layer upon the step. Essel and Tachie (2015) investigated surface roughness upon the upstream boundary layer and how that changes the shape of the wake, producing nominal changes for the purpose of this investigation.

The adapted Froude number Fr' is analogous to a densitometric Froude number Fr in that it relates inertial forces to buoyancy. A traditional densitometric Froude number ($Fr = U/\sqrt{g_0' H}$) can be found through inspection to be $Fr^2 = Fr'^3 \hat{q}_0$, and does not constitute a separate non-dimensional group. Since the exhaust is quickly diluted and mixed into the wake, the total buoyancy flux into the wake is more dynamically significant than the exhaust buoyancy strength and therefore Fr' was selected over Fr. As we see later, Fr' can also be considered as a ratio of the time scale associated with recirculation in the wake and the time scale associated with buoyancy-driven transport within the exhaust plume.

https://doi.org/10.1017/flo.2023.14 Published online by Cambridge University Press

Similarly, the dynamically significant quantity when non-dimensionalising the concentration downstream of the step is not the concentration of the exhaust c_0, but the concentration volume flux $c_0 q_0$. Therefore, a generic concentration (c_*) is non-dimensionalised with the selected repeating variables as

$$\hat{c}_* = \frac{c_* UH}{c_0 q_0} = \frac{c_*}{c_0 \hat{q}_0}. \tag{2.2}$$

We characterise the concentration behind the step using the average concentration $\bar{c}_{H\times H}$ in an $H \times H$ square immediately downstream of the step (figure 1*b*). When non-dimensionalised in accordance with (2.2), this averaged quantity is denoted as $\hat{c}$, such that

$$\hat{c} = \frac{\bar{c}_{H\times H}}{c_0 \hat{q}_0}. \tag{2.3}$$

We have chosen this measure $\bar{c}_{H\times H}$ as it can be clearly and objectively defined, i.e. it does not depend on the exact size or shape of the wake.

Invoking Buckingham's π-Theorem, we expect the functional relationship

$$\hat{c} = f\left(Re_H, \hat{q}_0, Fr'\right) \approx f(Fr'), \tag{2.4}$$

since we consider the Reynolds-invariant regime and the assumption that $\hat{q}_0 \approx 0$, except where it constitutes exhaust concentration flux, since the exhaust concentration is expected to be significantly higher than the average wake concentrations.

2.1. Modelling neutrally buoyant pollution dispersion

We begin modelling our flow by considering the neutrally buoyant case. We time-average the wake and simplify the system into three distinct regions: a well-mixed recirculation region, a shear layer and a free-stream flow (figure 1*a*). The fluxes of concentration between these three regions are modelled and balanced to estimate the average concentration within the recirculation region c_r. The shear layer and the recirculation vortex are coupled flow structures, with the shear layer driving the recirculation vortex and the vortex feeding into and drawing from the shear layer. From this point onward, the wake of the backward-facing step is separated into a structure resembling a shear layer bounding a low-velocity region below, referred to as the recirculation region.

The shear layer entrains fluid from the recirculation region and the free-stream flow. We parametrise the shear layer with a streamwise coordinate s. In the following, we neglect the effects of curvature of s on the entrainment and detrainment flows of the shear layer. At some point along s, the shear layer flow is drawn back (detrained) into the recirculation region. This point of entrainment reversal aligns with the centre of the primary vortex. We define this length along s until this entrainment reversal as s_1, and the distance from this point to the end of the shear layer as s_2 (figure 2). A careful inspection of our particle image velocimetry (PIV) velocity field measurements (figure 5) shows that the centre of the primary vortex aligns with the midpoint along the shear layer. This has motivated the modelling assumption

$$s_1 = s_2. \tag{2.5}$$

We model the entrainment velocity U_e into the shear layer as being of constant magnitude and proportional to the velocity difference between the midstream velocity and the free stream $\Delta U \approx U/2$. This allows the entrainment velocity to be expressed as

$$U_e = E\frac{U}{2}, \tag{2.6}$$

$$\hat{U}_e = \frac{U_e}{U} = \frac{E}{2}, \tag{2.7}$$

https://doi.org/10.1017/flo.2023.14 Published online by Cambridge University Press

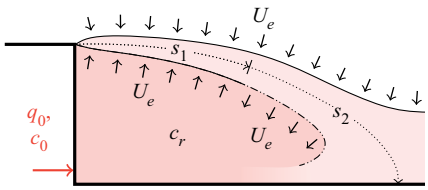

Figure 2. *The neutral case. Exhaust flow per unit depth q_0 is injected at the base of the step and well mixed into the recirculation region. Until point s_1 flow is entrained into the shear layer from the free stream and the recirculation region at rate U_e. Beyond s_1, until the point s_2, flow is entrained and detrained (as indicated) from the shear layer also at rate U_e. Points s_1 and s_2 are defined in § 2.1. The average value of pollutant concentration with the recirculation region is c_r. Diagram not to scale.*

where E is a constant entrainment coefficient, relating the entrainment velocity to the characteristic velocity deficit between the shear layer and the outside flow. Integrating this velocity over the length s_1 gives the total flux $U_e s_1$ across the surface. By considering conservation of volume within the recirculation region and using our modelling assumptions $\hat{q}_0 \approx 0$ and $s_1 = s_2$, we can conclude that the detrainment velocity U_d out of the shear layer into the recirculation region has the same value as U_e, i.e. $U_d = U_e$, with Appendix B.2 briefly discussing the the validity of this assumption.

Additionally considering the fluxes of concentration into the shear layer and recirculation region allows for the time-average concentration within the shear layer (c_{sl}) and the recirculation region (c_r) to be found (Appendix B.2). The average concentration within the recirculation region is given by

$$c_r|_{Fr'\to\infty} = c_0 \frac{\mathrm{e}^{1/2} q_0}{U_e s_1}, \tag{2.8}$$

$$\hat{c}_r|_{Fr'\to\infty} = \frac{c_r|_{Fr'\to\infty}}{c_0 \hat{q}_0} = \frac{\mathrm{e}^{1/2}}{\hat{U}_e \hat{s}_1}, \tag{2.9}$$

where $\hat{s}_1 = s_1/H$. As outlined in figure 1(*b*), we wish to estimate the average concentration within an $H \times H$ region. If we assume the exhaust is quickly well mixed into the recirculation region and that the recirculation region fills the $H \times H$ zone, $\hat{c}$ can be modelled as being equal to $\hat{c}_r|_{Fr'\to\infty}$.

2.2. Modelling buoyant pollution dispersion

We now examine the effect of introducing buoyancy. When introduced, the buoyancy forces compete against the inertial forces in the wake. As buoyancy becomes more influential, it is expected that the inertial forces within the recirculation region will be overcome and a wall plume will form on the backward face of the step. When buoyancy is sufficiently strong, the entrainment into the plume will prevent a pollutant from being mixed directly into the recirculation region, but instead will rise up and into the shear layer. When it reaches the shear layer, the considerably higher inertial forces present there take over and the pollutant gets mixed into and follows the behaviour of the shear layer (figure 3*a*).

As with the neutral exhaust, this scenario (figure 3*a*) can be modelled by considering volume and concentration fluxes into and out of the recirculation region, the shear layer and now additionally the plume. The entrainment flux per unit depth into the wall plume (q_{pe}) can be derived from the plume entrainment assumption (see Turner, 1973). As outlined in Appendix B.1, it is given by

$$q_{pe} = 3\alpha f_0^{1/3} H, \tag{2.10}$$

$$\hat{q}_{pe} = \frac{3\alpha}{Fr'}, \tag{2.11}$$

https://doi.org/10.1017/flo.2023.14 Published online by Cambridge University Press

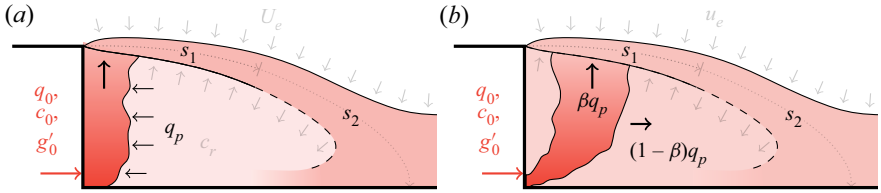

Figure 3. *The effect of a buoyant pollutant. (a) When buoyancy is sufficiently strong, a dominant wall plume will form on the back of the step. The total entrainment flux per unit depth into the wall plume is q_{pe}. Aspects of the model unchanged from the neutral exhaust model (2) are shown faded. The average values of concentration and buoyancy in the recirculation region are c_r, g_r'. (b) For slightly weaker buoyancy forcing, some of the pollutant will be mixed into the recirculation region as the plume rises. We denote the fraction of plume pollutant flux that reaches the shear layer as β. Diagrams not to scale.*

where α is the entrainment coefficient for the plume ($\alpha \approx 0.09$) and 3 is a constant relating the characteristic plume velocity to the buoyancy flux (Parker, Burridge, Partridge, & Linden, 2020).

There is a large range of intermediate behaviour where the exhaust buoyancy is not strong enough to overcome the inertial forces in the wake. In this range we model that a fraction $0 < \beta < 1$ of the plume pollutant will make it directly into the shear layer as a result of its buoyancy whilst the remaining proportion $(1-\beta)$ is mixed into the recirculation region. Determining β is key to modelling this intermediary behaviour. The value of β will depend upon the ratio between a time scale for how quickly the buoyant pollutant can rise to the height of the shear layer (τ_p) and a time scale for how quickly the recirculation region can mix the pollutant (τ_r). Through dimensional considerations these two time scales can be determined as

$$\tau_p \equiv \frac{H}{f_0^{1/3}}, \quad \tau_r \equiv \frac{H}{U}, \quad \text{where } \frac{\tau_r}{\tau_p} = \frac{U}{f_0^{1/3}} = Fr', \tag{2.12a,b}$$

where we note that $f_0^{1/3}$ is a characteristic velocity scale of a line plume. This suggests that β is a function of Fr', and exhibits the behaviour that $\beta \to 1$ as $Fr' \to 0$ and $\beta \to 0$ as $Fr' \to \infty$. A function that fits this behaviour is an exponential:

$$\beta = \exp(-Fr'/Fr_c'), \tag{2.13}$$

which is our modelling assumption for the functional dependence $\beta(Fr')$. Here, Fr_c' is a constant which can be thought of as a critical Froude number where the buoyancy forces match the inertial forces within the wake. This can be estimated by considering the flow speed within the wake, which from figure 5 can be seen to be approximately $0.03 < |\boldsymbol{u}|/U < 0.1$. This gives an estimate for the critical Froude number as $10 < Fr_c' < 30$.

Considering the concentration and volume fluxes into and out of the plume, the shear layer and the recirculation region (Appendix B), the normalised average pollutant concentration within the recirculation region can be found as a function of Fr' to be

$$\hat{c}_r = \frac{D(Fr') - \beta(Fr')}{\beta(Fr')\hat{q}_{pe} + \hat{U}_e\hat{s}_1}, \tag{2.14}$$

where $\hat{q}_{pe} = q_{pe}/(UH)$ and D is defined further below in (2.16*a–d*).

We wish to estimate the average concentration within an $H \times H$ region immediately behind the step. As outlined in more detail in Appendix B.2, the fraction of the exhaust plume β that is driven into the shear layer due to the buoyancy of the plume will also contribute to the total concentration during the period of time it takes the plume to rise to the shear layer. By assuming that the plume remains located within the $H \times H$ region, this contribution can be found to be $\beta Fr'/3$ when averaged over the $H \times H$

https://doi.org/10.1017/flo.2023.14 Published online by Cambridge University Press

region. By assuming that the recirculation region fills the $H \times H$ zone, the prediction for $\hat{c}$ is then given by

$$\hat{c} = \frac{\bar{c}_{H\times H}}{c_0 \hat{q}_0} = \frac{D - \beta}{\beta \hat{q}_{pe} + \hat{U}_e \hat{s}_1} + \frac{\beta}{3} Fr', \tag{2.15}$$

$$D(Fr') = \exp\left(\frac{\beta \hat{q}_{pe} + \hat{U}_e \hat{s}_1}{\beta \hat{q}_{pe} + 2\hat{U}_e \hat{s}_1}\right), \quad \beta(Fr') = \exp(-Fr'/Fr'_c), \quad \hat{q}_{pe}(Fr') = \frac{3\alpha}{Fr'}, \quad \hat{U}_e = \frac{E}{2}, \tag{2.16a–d}$$

with α being the entrainment coefficient for the plume and E being the entrainment coefficient for the shear layer. The assumption that the recirculation region encompasses the $H \times H$ area is reasonable since the dip of the shear layer is very low for the majority of the shear layer as can be seen from PIV measurements in figure 5. As the shear layer develops, its width increases. This means that the shear layer slightly encroaches on the $H \times H$ region. However, the contribution of this encroachment is negligible and can be calculated to have an influence of less than 0.5 % upon the predicted value of $\hat{c}$.

As $Fr' \to 0$ the value of $\hat{c}$ predicted by (2.15) approaches zero as $\hat{q}_{pe} \to \infty$ according to (2.16*a–d*) . At particularly low Froude numbers, the modelling assumptions will loose their validity: decreasing Fr' by changing U or g'_0 causes problems to arise with Reynolds invariance and the Boussinesq approximation, respectively. Increasing the exhaust flow rate per unit depth (q_0) will break the assumption that q_0 is small and does not influence the flow structure.

3. Experimental methods

We now describe the experiments performed to test the model from the previous section. Experiments were performed within a recirculating water flume (figure 4*a*) with a working cross-section of 300 mm × 450 mm and flow speeds in the range of 73–133 mm s^{-1}. Two turbulence-damping meshes were placed upstream to improve the flow uniformity in the working section. The upstream contraction and the blockage ratio (10 %) meet the criteria detailed by Barlow, Pope, and Rae (1999) for maximum allowable blockage ratio within wind tunnels and water flumes. As shown in figure 4(*b*), the step is smoothly ramped up to its full height over a distance of 205.8 mm (~4.5H) and then maintained at the full step height for 67 mm (~1.5H). The step spans the entire width of the flume, which gives an aspect ratio of $AR = 6.7$. Brederode and Bradshaw (1973) and Papadopoulos and Otugen (1995) investigated the influence of AR upon the reattachment length, both finding that reattachment length increases with AR until it levels off to a consistent value, occurring around $AR = 5$, this also being a function of the expansion ratio of the step. With non-infinite aspect ratios, three-dimensional flow structures are still present, and Hall, Behnia, Fletcher, and Morrison (2003) find that the primary and secondary vortices spiral up to meet the top of the step at the sidewalls when observing a time-averaged flow structure. Brederode and Bradshaw (1973) considered an expansion ratio of $ER = 1.11$, equal to that considered within this investigation, and found the reattachment length stabilised to 5.9.

The step is mounted on a Perspex floor which is 600 mm long and the full width of the tank. A gear pump is used to pump a dyed saline solution through a line source at the base of the step (figure 4*c*). The tested values of q_0, the volume flux per unit depth, were 12.3, 17.4, 22.6 and 27.9 mm^2 s^{-1}, which when combined with the range of flow speeds tested results in a range of $2.1 < \hat{q}_0 < 8.5$ for the normalised exhaust flow rate per unit depth. The line source exhaust (figure 4*c*) was designed to trip the exhaust to turbulence, inspired by the Cooper plume nozzle (Kaye & Linden, 2004). The exhaust was passed initially through a brass plate with 1 mm diameter holes drilled at a spacing of 7 mm.

The saline exhaust used in this investigation is negatively buoyant in comparison with the water used as the working fluid. The step and Perspex floor, as shown in figure 4(*a*), are inverted and as such are representative of a positively buoyant plume released behind an upward-facing step. We assume the flow is Boussinesq, i.e. that density differences are small and have negligible influence except where the difference is multiplied by acceleration due to gravity, g. The experimental results are presented flipped, as many applications involve positively buoyant pollutants behind an upward-facing step.

https://doi.org/10.1017/flo.2023.14 Published online by Cambridge University Press

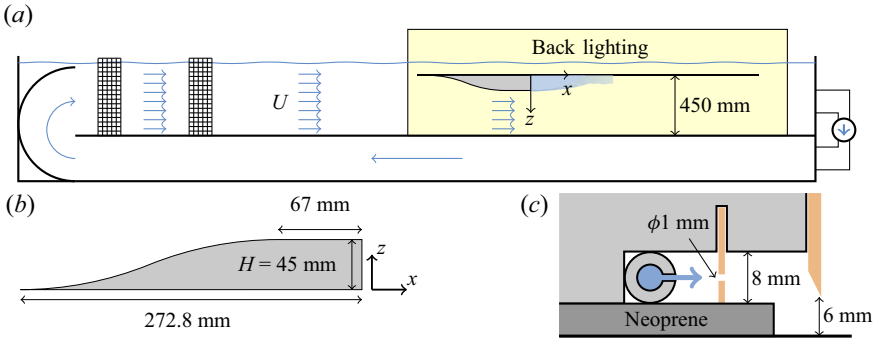

Figure 4. *Experimental set-up. (a) The recirculating flume has a* 300 mm × 450 mm *cross-section and flow speeds of* 73–133 mm s^{-1}. *(b) The step smoothly ramps up to a height* $H = 45$ mm *over a distance* ~4.5H *and remains at a constant height for* ~1.5H *giving an expansion ratio of* 1.11. *Flow rates of* $12.3 < q_0 < 27.9$ mm^2 s^{-1} *were used giving* $0.015 < U_0/U < 0.064$, *where* U_0 *is the speed of the exhaust flow and* U *the free-stream flow speed. (c) Line source design. Exhaust passes through a brass plate with* 1 mm *diameter holes drilled at a spacing of* 7 mm. *Flow then exits through a sharp-edged* 6 mm *gap at the base of the step.*

Quantitative data were collected using PIV and dye attenuation measurements. The PIV technique was used to measure the velocity field behind the step in order to identify when the wake structure became Reynolds invariant. The PIV used 55 µm diameter neutrally buoyant polyamide particles and data were collected at 50 fps and analysed with PIVlab (Thielicke & Sonntag, 2021). A high-performance signal synchroniser was used to provide a stable DC power supply to the PIV light sheet. Flickering interference between the 50 fps frame rate and the 50 Hz mains AC power supply was not found to occur.

Back-lit dye attenuation, as outlined by Allgayer and Hunt (2012), is used to extract depth-integrated concentration profiles of the released 'pollutant'. Dye attenuation data were collected at 20 fps. A methylene blue dye concentration of 0.447 mg l^{-1} was used. A description of the methods used, along with calibration curves and ranges of assumed linearity for the dye can be found in Appendix A.1. Further details of uncertainties in experimental measurements can be found in Appendix A.2.

As we are principally interested in applications at high Reynolds number, we performed a series of experiments to ensure our experiments were in the Reynolds-number-invariant regime. Armaly et al. (1983) and Nadge and Govardhan (2014) both examined the backward-facing step at varying Reynolds numbers, finding that the reattachment length was Reynolds invariant around $Re_H \sim 2 \times 10^4$ for an expansion ratio of 1.1 (equal to the expansion ratio examined in this paper). Tihon et al. (2012) also investigated the behaviour of reattachment length with Reynolds number, and found a sharp increase in reattachment length at low Re_H which levels out around $Re_H = 800$–1200. Our experiments were performed at a higher Re than that of Tihon et al. (2012), but lower Re than that of Armaly et al. (1983) and Nadge and Govardhan (2014); therefore, we include PIV results demonstrating Re_H invariance.

We varied the Reynolds number in the range $370 < Re_H < 6000$, with PIV results for five selected Reynolds numbers shown in figure 5. There is a significant change to the general flow structure between $Re_H = 370$ and $Re_H = 880$ (figure 5*a*,*b*) with significantly fewer changes as Re_H increases to 3300, 4600 and 5300 (figure 5*c*–*e*). The reattachment length reached follows the pattern outlined by Tihon et al. (2012) and our PIV experiments indicate that the overall structure of the wake behind the backward-facing step has reached Reynolds invariance at $Re_H \approx 3000$. This can further be seen by considering the change to the recirculation length with Reynolds number, see figure 5(*f*), in which the recirculation length reduces and plateaus at approximately 4.7H. All subsequent experiments were performed above the determined critical Reynolds number, with experiments performed at $Re_H = 3300$, 4600 and 6000.

https://doi.org/10.1017/flo.2023.14 Published online by Cambridge University Press

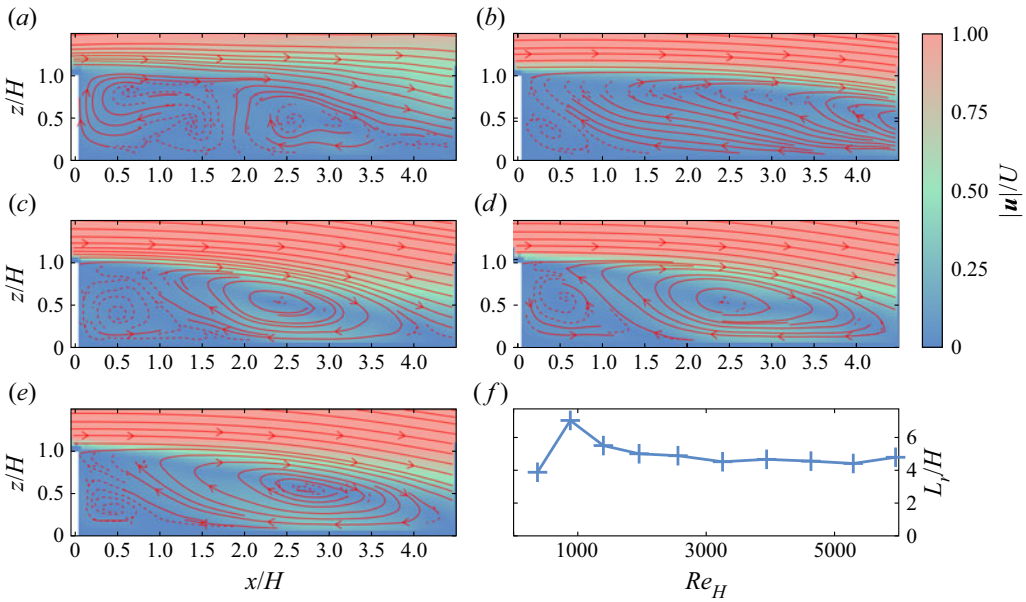

Figure 5. *Reynolds number effects. (a–e) Time-averaged velocity profiles with streamlines for increasing Reynolds number* $Re_H = [370, 880, 3300, 4600, 5300]$. *Free-stream flow speeds* $U = [8, 20, 73, 103, 118]$ mm s^{-1}. *Dashed streamlines indicate* $|\boldsymbol{u}| < 0.1U$, *where* $\boldsymbol{u}$ *is the local flow velocity. (f) Recirculation length* (L_r) *plotted against Reynolds number. Invariance is observed for* $Re_H \gtrsim 3000$.

4. Results

We now outline the experimental results. Figure 6(*a*,*c*,*e*) shows instantaneous false-colour concentration fields for three selected cases. Buoyancy has been introduced in the second, and increased further in the third. The profiles are produced using a dye attenuation technique (details in Appendix A.1), which results in depth averaging over the width of the flume. The shear layer confining the recirculation region can be observed with instabilities developing on the upper edge similar in appearance to classic Kelvin–Helmholtz instabilities, although they cannot be directly described as Kelvin–Helmholtz (except in the neutral exhaust case) due to the presence of an unstable density stratification in the direction of shear (see the supplementary information for videos available at https://doi.org/10.1017/flo.2023.14). As buoyancy is increased, less of the pollutant is trapped within the recirculation region, and instead is quickly transported up to the shear layer by the plume.

Figure 6(*b*,*d*,*f*) shows time-averaged concentration fields for the three cases considered. The profiles were time-averaged over 90 s. The convergence of these profiles was checked by increasing the averaging time until the mean concentration within an $H \times H$ region behind the step had stabilised. This was found to converge after ~45 s. Streamlines, derived from PIV from experiments performed at similar Froude numbers ($Fr' = [\infty,\ 10.9,\ 7.1]$), have been overlaid on the concentration fields. The macrostructure of the wake is unchanged through the addition of buoyancy. Small changes between the three profiles can be noted close to and towards the base of the step. It should be noted that this coincides with the region where the PIV is less accurate due to the combination of significantly slower flow speeds and refractive index issues relating to the salinity of the exhaust.

From figure 6(*b*), it can be seen that at high Fr' the pollutant becomes close to well mixed within an $H \times 1.5H$ rectangle behind the wake, with pollutant transport dominated by the inertial forces of the recirculation region. The pollutant is eventually pushed up into the shear layer by the strong primary vortex. As the Fr' number decreases, the strength of the buoyancy begins to overcome the inertial forces in the wake and buoyancy transports the pollutant directly into the shear layer rather than being mixed

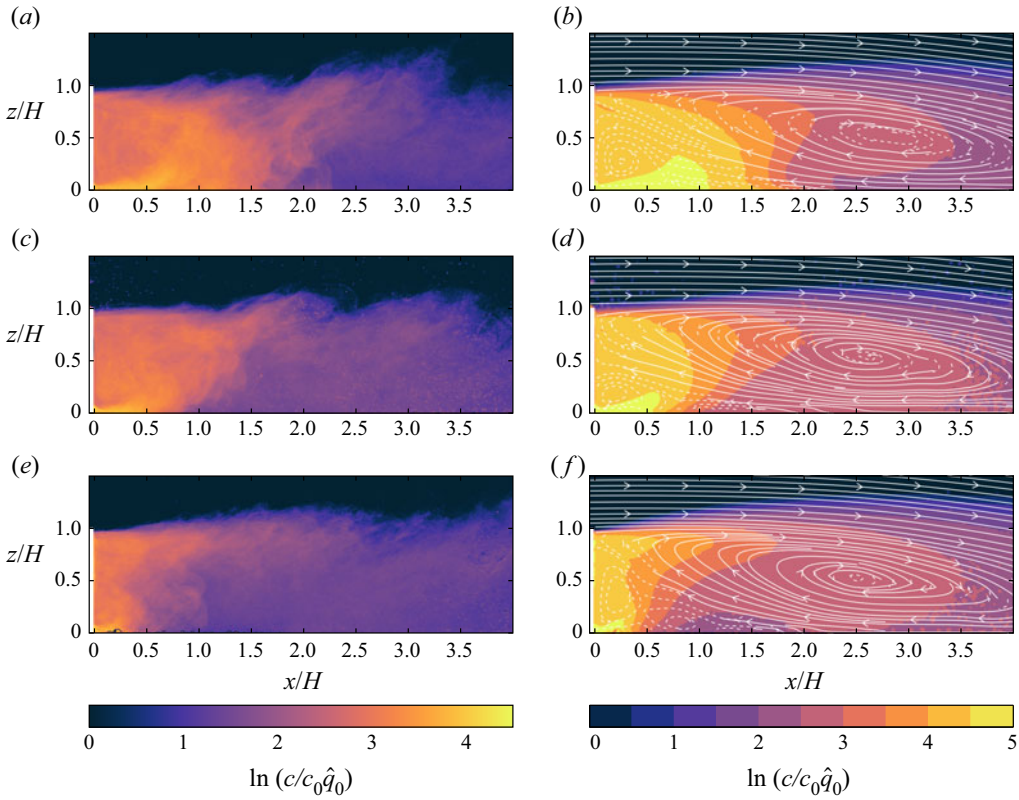

Figure 6. *(a,c,e) Instantaneous concentration fields (using a natural logarithmic scale) and (b,d,f) time-averagedconcentration fields (using a logarithmic scale) with PIV streamlines overlaid, for varying adapted Froude number* $Fr' = U/(q_0 g_0')^{1/3}$*: (a,b)* ∞*; (c,d)* 9.9*; (e,f)* 6.4*. The flow speed was* $U = 73\,\mathrm{mm\,s^{-1}}$ *(*$Re_H = 3300$*) and the exhaust flow rate (per unit depth)* $q_0 = 27.9\,\mathrm{mm^2\,s^{-1}}$*. The buoyancy of the pollutant was varied as* $g_0' = [0, 14.3, 51.7]\,\mathrm{mm\,s^{-2}}$*.*

into the recirculation region (figure 6*d*). As the Fr' number is decreased further, the buoyant pollutant sticks more closely to the wall of the step, forming a structure analogous to a wall plume (figure 6*f*). At intermediary stages, the buoyant plume attaches and detaches due to unsteady fluctuations in the inertial forces in the wake. This behaviour will also be dependent upon the exhaust momentum, an effect we have neglected in this investigation. The velocity scales within the recirculation region are significantly lower than those in the free stream and the shear layer (see figure 5); therefore as the influence of buoyancy is increased it first overcomes the inertial forces within the recirculation region. We expect that as buoyancy is increased further, it will begin to influence the shear layer and macrostructure of the wake; however, this was not clearly observed experimentally within the range of Fr' that we were able to achieve while keeping the experiment in the Reynolds (Re_H)-invariant regime. The neutral exhaust flow in figure 6(*b*) might appear to show a strong exhaust jet which clings to the floor up until approximately H, which would contradict the previous assumption that the exhaust momentum is negligible. However, the strength of this exhaust jet is exaggerated by the secondary recirculation vortex which pushes pollutant in the direction of the exhaust jet. As buoyancy is increased in figure 6(*d*,*f*) and buoyancy begins to overcome the inertial forces in the secondary vortex, the jet width reduces to $0.25H$.

The effect of Fr' can be seen further in figure 7, which shows vertical profiles of time-averaged concentration at three distances from the step with increasing Fr'. These profiles can be thought of as vertical lines taken from figure 6(*b*,*d*,*f*). The highest buoyancy case (lowest Fr', yellow) has a reduced

https://doi.org/10.1017/flo.2023.14 Published online by Cambridge University Press

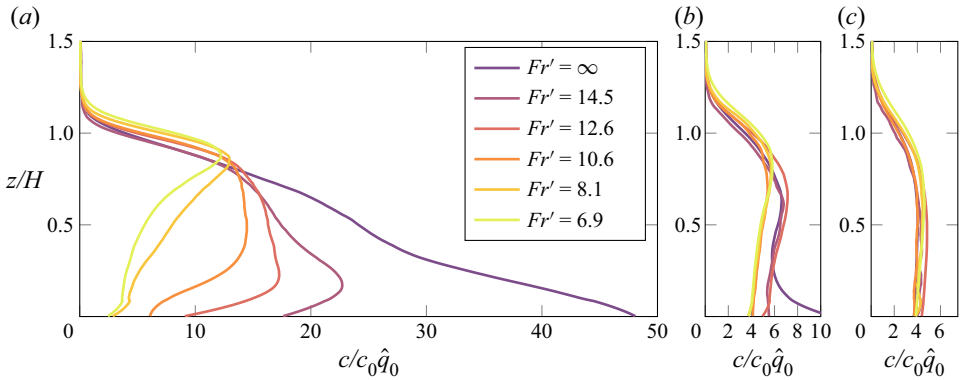

Figure 7. *Vertical profiles of concentration at varying distances downstream of the step: (a) $x/H = 1$, (b) $x/H = 2$ and (c) $x/H = 3$. All x axes have equal proportioned scales. The flow rate was $U = 73\,\mathrm{mm\,s^{-1}}$ and the exhaust flow rate per unit depth was $q_0 = 22.6\,\mathrm{mm^2\,s^{-1}}$. The Froude number was varied by changing the buoyancy as $g_0' = [0,\ 5.54,\ 8.45,\ 14.3,\ 31.9,\ 51.7]\,\mathrm{mm\,s^{-2}}$.*

concentration trapped immediately behind the step compared with the lowest and neutral buoyancy (high Fr', purple). This reduction is consistent from $x/H = 1$ to $x/H = 3$ (figure 7*a*,*c*), although further from the step the relative reduction in concentration is smaller. Furthermore, there is a noticeable shift upwards in the location of the peak concentration behind the step as buoyancy increases. Initially, because the pollutant is being advected and dispersed by the recirculation region, a fairly flat distribution is observed with the neutral case showing a peak concentration very low to the ground. As the influence of buoyancy increases (Fr' decreases) the wall plume develops and pushes the pollutant into the shear layer, shown through the presence of a distinct peak occurring around $z/H \sim 0.8$ at $x/H = 1$. At still lower Fr' it is expected that this peak would move upwards as the strength of the buoyancy within the shear layer begins to overcome the inertial forces of the shear layer.

The reduction in pollutant trapped behind the step can be quantitatively examined by averaging the concentration in an $H \times H$ square behind the step ($\bar{c}|_{H\times H}$). Figure 8 shows $\hat{c}$ plotted against the adapted Froude number Fr', where $\hat{c}$ is $\bar{c}|_{H\times H}$ divided by $c_0\hat{q}_0$ as defined in (2.1*a–c*). The data points in figure 8 represent a systematic variation of the exhaust buoyancy ($g_0' = [0,\ 5.54,\ 8.45,\ 14.3,\ 31.9,\ 51.7]\,\mathrm{mm\,s^{-2}}$), the exhaust flow rate ($q_0 = [12.3,\ 17.4,\ 22.6,\ 27.9]\,\mathrm{mm^2\,s^{-1}}$) and the free-stream flow speed ($U = [73,\ 103,\ 133]\,\mathrm{mm\,s^{-1}}$).

Figure 8(*a*) shows the average concentration behind the step against the buoyancy flux. Figure 8(*b*) shows how these data collapse onto a curve displaying the asymptotic behaviour predicted by the theory developed in § 2. The dashed line shows the model from (2.15) and (2.16*a–d*) with the parameters E, α and Fr_c' fitted with a least-squares method to the data. A comparison between the predicted values and the fitted values can be found within table 1. Parameter $\hat{s}_1$ is taken as half the length of the shear layer, which is taken to be half of the length of the recirculation region.

The exhaust flow rate was assumed to be small ($\hat{q}_0 \ll 1$). To check the validity of this assumption, we can substitute the range of values for $\hat{q}_0$ used into the model. We find this changes the estimate for $\hat{c}$ by a maximum of 4 %.

5. Conclusions and discussion

We have investigated the effect of buoyancy on pollutant dispersion behind a backward-facing step. We have identified the transition between two main regimes, depending on the relative strength of the buoyancy of the pollutant and the inertia of the surrounding flow, as measured by an adapted Froude number, Fr'. When the effect of buoyancy is weak ($Fr' \gtrsim 25$) pollutant dispersion is driven entirely by

https://doi.org/10.1017/flo.2023.14 Published online by Cambridge University Press

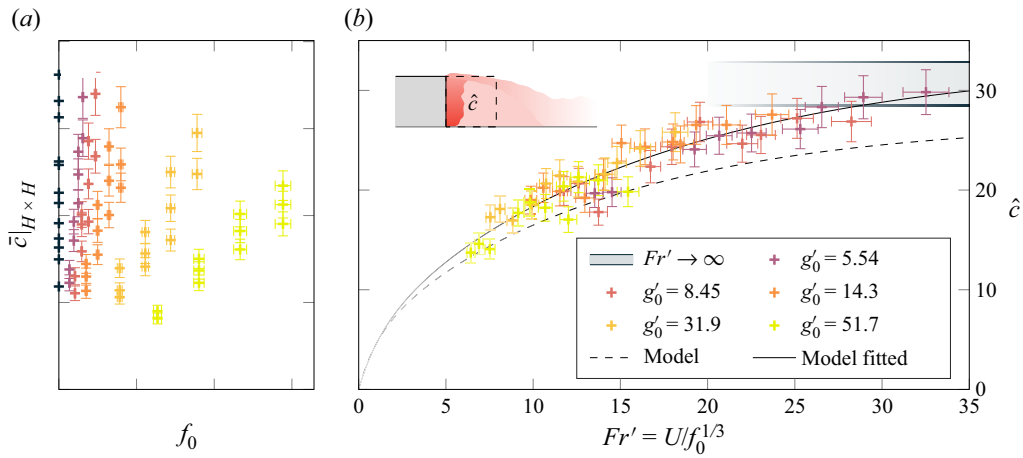

Figure 8. *The effect of buoyancy on the concentration of pollutant trapped behind a step. (a) Average concentration within an $H \times H$ region behind the step plotted against exhaust buoyancy flux. (b) Average non-dimensional concentration $\hat{c}$ behind the step versus the adapted Froude number Fr'. The flow speed was varied as $U = [73\ 103\ 133]\,\mathrm{mm\,s^{-1}}$ along with the exhaust flow rate per unit depth as $q_0 = [12.3\ 17.4\ 22.6\ 27.9]\,\mathrm{mm^2\,s^{-1}}$ and the exhaust buoyancy as $g_0' = [$see legend$]\,\mathrm{mm\,s^{-2}}$. Dashed line represents model (2.15) with expected model parameter values and solid line shows the model with fitted parameter values (see table 1).*

Table 1. *Model parameters. Comparison of predicted with fitted values. Fit performed with a least-squares method, and values shown to two significant figures.*

Parameter	Expected value	Fitted value
E	0.051^a	0.041
α	0.090^b	0.099
Fr_c'	$10\text{–}30^c$	23.2

[a]Derived from Rajaratnam (1976).
[b]Turner (1973) and Parker et al. (2020).
[c]Expected range from order-of-magnitude considerations in § 2.2.

advection in the wake (figure 9*a*). As the buoyancy of the pollutant is increased (moderate $Fr' \lessapprox 15$), buoyancy-driven convection dominates relative to inertial forces within the recirculation region but remains negligible in comparison with the inertial strength of the shear layer (figure 9*b*). As a result, in this regime the pollutant trapped behind the step reduces, but the shape of the wake is unaffected. A third regime is hypothesised to exist below the range of Fr' tested in our study ($7 < Fr' < \infty$) where buoyancy becomes sufficiently strong to influence the height of the shear layer and the overall shape of the wake (figure 9*c*).

A theoretical steady-state model was developed to determine the average pollutant concentration held within the recirculation region and how it changes with Fr'. The model predicts the pollutant trapped in this region to decrease as the influence of buoyancy is increased (decreasing Fr'). The experimental results were found to compare well with the model predictions, with three fitted parameters. The values of these fitted parameters were close to estimates derived from further modelling.

This paper has begun to quantify how buoyancy changes the dispersion and transport of a pollutant whilst also subject to the inertial forces in the wake of a backward-facing step. This work can feed into

https://doi.org/10.1017/flo.2023.14 Published online by Cambridge University Press

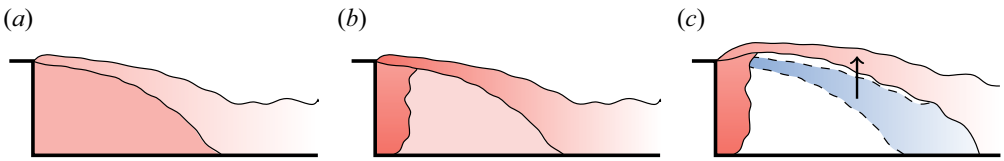

Figure 9. *Three regimes. (a) High Fr′: pollutant is advected and dispersed by the recirculation region. (b) Moderate Fr′: a wall plume develops and feeds directly into shear layer. The concentration of pollutant trapped behind the step decreases. (c) Low Fr′: increasing buoyancy starts to influence the shape of the wake and location of the shear layer.*

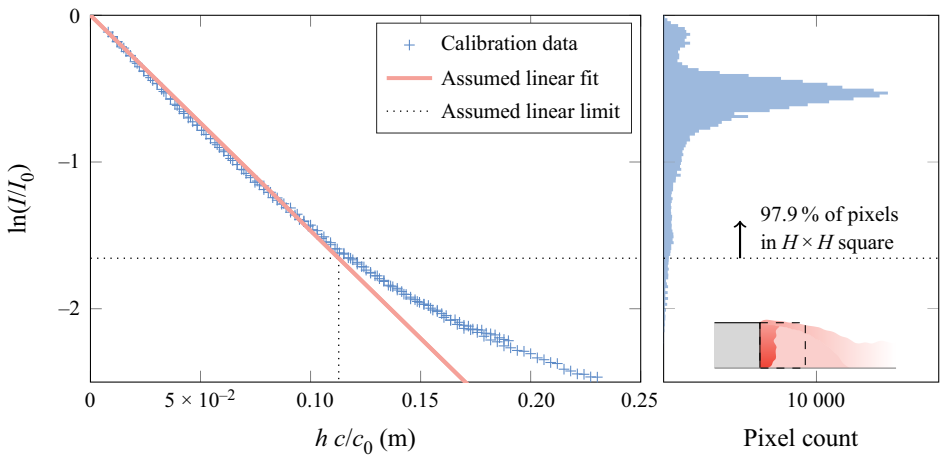

Figure 10. *Methylene blue calibration curve and histogram of pixel values within an instantaneous shot of the $H \times H$ region behind the step with a neutral exhaust being expelled. Here c_0 has a methylene blue concentration* $0.447\ \mathrm{mg\,l^{-1}}$*, with this calibration curve being specific to the lighting, camera and camera settings of this investigation.*

future research into the effect of buoyancy on car exhaust dispersion, along with other important urban pollution transport problems, such as the dispersal of pollution behind buildings.

Appendix A. Experimental methods

A.1. Dye calibration

The dye (methylene blue) used to extract approximate pollutant concentrations through dye attenuation does not perfectly follow the assumed Lambert–Beer attenuation law:

$$\ln\left(\frac{I}{I_0}\right) \propto -hc, \tag{A.1}$$

where I is the light intensity recorded by the camera, I_0 is the background light intensity (Allgayer & Hunt, 2012), h is the depth of the attenuating specimen and c is the dye concentration. Nonlinearity is introduced due to a range of wavelengths of light being used during the experiment, an appropriate red filter being used to minimise this. The actual attenuation and the assumed range of linearity are shown in figure 10.

Figure 10 also displays a histogram showing the distribution of pixel values of $\ln(I/I_0)$ within an $H \times H$ square behind the step for an instantaneous snapshot of a neutral exhaust experiment. It can

https://doi.org/10.1017/flo.2023.14 Published online by Cambridge University Press

Table 2. *Errors associated with fundamental measured quantities.*

	U (cm s^{-1})	ρ (g cm^{-3})	Q_0 (ml min^{-1})	H (mm)	W (mm)
Value	7.3–13.3	0.999–1.006	250–550	45	300
Absolute error	$0.0129U$	5×10^{-6}	5	1	10
Percentage error	0.577	$\sim 5 \times 10^{-4}$	0.9–2	2.2	3.3

be found that 97.9 % of pixel values fall within the assumed range of linearity. The total error for the estimated average concentration within an $H \times H$ square ($\hat{c}$) can be calculated from the two plots in figure 10 and found to be 4.9 % due to nonlinearity in dye attenuation.

A.2. Error analysis

Table 2 lists the parameters considered within this investigation, the range of values considered and absolute errors associated with each value. From this the percentage errors for each quantity can be found and combined to find the errors associated with the final presented quantities.

Appendix B. Modelling the wake

B.1. Modelling the plume

The plume is modelled as if it is acting in an ambient and still environment.

Entrainment velocity into the plume is proportional to the characteristic plume velocity, related by the entrainment constant α (Turner, 1973). The velocity within a wall plume is assumed to be self-similar and proportional to the cube root of exhaust buoyancy flux $f_0^{1/3}$ with a proportionality factor of 3 (Parker et al., 2020; Turner, 1973). Integrating this for $0 < z < H$ gives the total plume entrainment flux per unit depth as

$$q_{pe} = 3\alpha f_0^{1/3} H, \tag{B.1}$$

$$\hat{q}_{pe} = \frac{q_{pe}}{UH} = \frac{3\alpha}{Fr'}, \tag{B.2}$$

where $\hat{q}_{pe}$ is the normalised plume entrainment flux. Evaluating the volume and concentration fluxes into the plume, the volumetric flux (q_p) and average concentration (c_p) at the top of the plume after entrainment can be found to be

$$q_p = q_{pe} + q_0 \approx q_{pe}, \tag{B.3}$$

$$c_p = \frac{q_{pe} c_r + q_0 c_0}{q_p}. \tag{B.4}$$

In § 2.2, we outline that we expect a certain proportion of the plume (βq_p) to rise directly into the shear layer as a result of the plume buoyancy with the remaining fraction ($[1 - \beta] q_p$) being mixed back into the recirculation region (see figure 3*b*).

When estimating the average concentration $\bar{c}_{H\times H}$ within the $H \times H$ region (2.15), the contribution of the pollutant that is held within the plume that will not be well mixed into the recirculation region needs to be considered. At each time point, the plume transports directly into the shear layer a fraction $\beta c_0 q_0$ of the exhaust pollutant flux (the contribution $\beta c_r q_{pe}$ is accounted for in Appendix B.2). The total additional pollutant amount due to the plume (C_p) can be estimated using the exhaust flow rate multiplied

https://doi.org/10.1017/flo.2023.14 Published online by Cambridge University Press

by the time scale associated with how long it takes the plume to reach the top of the step. This gives

$$C_p = \beta c_o q_0 \frac{H}{3f_0^{1/3}}, \tag{B.5}$$

$$\hat{C}_p = \beta \frac{U}{f_0^{1/3}} \frac{H^2}{3} = \beta \frac{Fr' H^2}{3}, \tag{B.6}$$

where $3f_0^{1/3}$ is the characteristic velocity associated with a wall plume (Parker et al., 2020) and $\beta = \beta(Fr')$ accounts for the proportion of the plume that is expected to reach the shear layer without being mixed into the recirculation region (see (2.13)). Equation (2.15) considers the average pollutant concentration within the $H \times H$ region. Assuming that the plume remains within this region, the average contribution due to the plume can be found to be

$$\hat{c}_p = \beta \frac{Fr'}{3}. \tag{B.7}$$

B.2. Modelling the shear layer and recirculation region

In this section, we consider the fluxes into and out of the shear layer in order to determine the concentration profile within the shear layer. This will allow the average concentration c_r within the recirculation region to be calculated. We consider the general case where a fraction β (2.13) of the exhaust plume rises directly into the shear layer due to the buoyancy of the exhaust, with the remaining fraction $1 - \beta$ being well mixed into the recirculation region. To consider the neutral case, we set $\beta = 0$. We make the assumption that the exhaust volumetric flux is small in comparison with other volume fluxes, except where it contributes to the exhaust concentration flux, such that

$$q_0 \ll q_*, \quad q_0 c_0 \sim q_* c_*, \tag{B8a,b}$$

where q_* and c_* represent generic volume fluxes and concentrations considered within this investigation. The following modelling could be performed without the assumption that q_0 is small; however, the modelling assumption that the exhaust does not alter the flow structure would no longer be valid and further complex modelling would be required.

Figure 11(a) shows a control volume outlining the fluxes into and out of the shear layer up until the flow reversal point s_1. Balancing these fluxes, we can find the average flow rate and average concentration within the shear layer at s_1 to be

$$q_{sl}(s_1) = \beta q_{pe} + 2U_e s_1, \tag{B9}$$

$$c_{sl}(s_1) = \frac{\beta c_0 q_0 + c_r(\beta q_{pe} + U_e s_1)}{\beta q_{pe} + 2U_e s_1}. \tag{B10}$$

After point s_1, the flow is detrained out of the shear layer and back into the recirculation region. We assume here that the detrainment velocity U_d out of the shear layer into the recirculation region has the same magnitude as the entrainment velocity, namely $U_d = U_e$. Figure 11(b) shows the fluxes into and out of a small control volume of length ds after the point of entrainment reversal s_1. By considering this small control volume and a new streamwise coordinate ($s' = s + s_1$), we can derive the average shear layer concentration c_{sl} after the flow reversal as a function of s':

$$c_{sl}(s') = c_{sl}(s_1) \exp\left(-\frac{U_e s'}{q_{sl}(s_1)}\right). \tag{B11}$$

https://doi.org/10.1017/flo.2023.14 Published online by Cambridge University Press

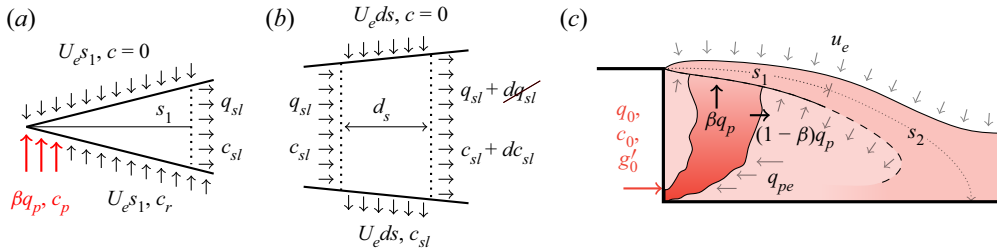

Figure 11. *Simplified shear layer control volumes, where q_{sl} is the shear layer volume flux, c_{sl} is the average shear layer concentration, U_e is the entrainment velocity, c_r is the average recirculation region concentration and c_0 and q_0 are the exhaust concentration and flow rate per unit depth. (a) Control volume before entrainment reversal, valid over length s_1. (b) Small control volume after entrainment reversal, valid over length s_2. (c) Wake control volumes. This figure is a collation of figures 2, 3(a) and 3(b). Not to scale.*

Integrating the detrainment velocity multiplied by $c_{sl}(s')$ over the length s_2 gives the total concentration flux from the shear layer into the recirculation region:

$$\int_0^{s_2} c_{sl} U_e \, \mathrm{d}s' = c_{sl}(s_1) q_{sl}(s_1) \left[1 - \exp\left(-\frac{U_e s_2}{q_{sl}(s_1)} \right) \right] \tag{B12}$$

$$= \left[\beta c_0 q_0 + c_r (\beta q_{pe} + U_e s_1) \right] \left[1 - \exp\left(-\frac{U_e s_2}{q_{sl}(s_1)} \right) \right]. \tag{B13}$$

Balancing the concentration fluxes into and out of the recirculation region,

$$\underbrace{c_r q_{pe}}_{\textit{Entrainment into plume}} + \underbrace{c_r U_e s_1}_{\textit{Entrainment into shear layer}} = \underbrace{\int_0^{s_2} c_{sl} U_e \, \mathrm{d}s'}_{\textit{Detrainment}} + \underbrace{(1-\beta)(q_{pe} c_r + co q_0)}_{\textit{Fraction of plume mixed into RR}}, \tag{B14}$$

see figure 11(*c*), an expression for the normalised average concentration within the recirculation region $\hat{c}_r$ can be found as

$$\hat{c}_r = \frac{c_r}{c_0 \hat{q}_0} = \frac{D - \beta}{\beta \hat{q}_{pe} + \hat{U}_e \hat{s}_1}, \tag{B15}$$

where

$$D = \exp\left(\frac{\hat{U}_e \hat{s}_2}{\hat{q}_{sl}(s_1)} \right) = \exp\left(\frac{\hat{U}_e \hat{s}_2}{\beta \hat{q}_{pe} + 2\hat{U}_e \hat{s}_1} \right). \tag{B16}$$

By considering conservation of volume within the recirculation region, we can relate the length $\hat{s}_2$ to $\hat{s}_1$ as

$$\hat{U}_e \hat{s}_2 = \hat{U}_e \hat{s}_1 + \beta \hat{q}_{pe}, \tag{B17}$$

therefore simplifying the expression for D to

$$D = \exp\left(\frac{\beta \hat{q}_{pe} + \hat{U}_e \hat{s}_1}{\beta \hat{q}_{pe} + 2\hat{U}_e \hat{s}_1} \right). \tag{B18}$$

Note that for the case of the neutral exhaust $\beta = 0$, we recover $\hat{s}_1 = \hat{s}_2$.

As outlined in § 2 and figure 1(*b*), we wish to estimate the average concentration $\bar{c}_{H\times H}$ within an $H \times H$ region immediately behind the step. The fraction of the exhaust concentration flux $\beta c_0 q_0$ that is driven

https://doi.org/10.1017/flo.2023.14 Published online by Cambridge University Press

directly into the shear layer due to the buoyancy of the plume also contributes to the total concentration $\bar{c}_{H\times H}$ during the period of time it takes for the plume to rise to the shear layer; see (B.5). It should be noted that the plume also contains the contribution $(1-\beta)c_0q_0$. However, this contribution is already taken into consideration when calculating c_r, see (B14), allowing an estimate for the total concentration:

$$\hat{c} = \frac{\bar{c}_{H\times H}}{c_0\hat{q}_0} \tag{B19}$$

$$= \hat{c}_r + \hat{c}_p \tag{B20}$$

$$= \frac{D-\beta}{\beta\hat{q}_{pe} + \hat{U}_e\hat{s}_1} + \frac{\beta}{3}Fr', \tag{B21}$$

where we used (B.7) and (B15). Here, if we consider the neutral exhaust ($Fr' \to \infty$ and $\beta = 0$) the following value of c_r is produced:

$$\hat{c}|_{Fr'\to\infty} = \frac{\mathrm{e}^{1/2}}{\hat{U}_e\hat{s}_1}. \tag{B22}$$

As $Fr' \to 0$, the value of $\hat{c}$ predicted by (B21) approaches zero ($\hat{q}_{pe} \to \infty$; see (B.2)). As outlined within the main body of the text (§ 2.2), it is expected that the model assumptions do not describe the behaviour at very low Fr' due to the exceptionally high exhaust buoyancy needed to produce low values of Fr'.

An assumption of this model is that the detrainment velocity U_d along the streamwise distance s_2 from the shear layer back into the recirculation region is equal to the entrainment velocity U_e along s_1, i.e. $U_d = U_e$, and both do not vary with s. For the neutrally buoyant case, this implies $s_1 = s_2$.

We now briefly consider what happens if the assumption $U_d = U_e =$ const. is dropped. There are two main mechanisms which could invalidate this assumption.

First, we consider the case where the entrainment velocity scale changes as the shear layer develops, i.e. the assumption of invariance with s is dropped. This might be expected since the flow that is drawn back into the recirculation region will provide a non-zero lower velocity boundary condition along s_2. We thus consider that along s_2, there is a simultaneous increase in the magnitude of entrainment velocity $U_{e,s_2} > U_e$ and the detrainment velocity $U_d = U_{e,s_2}$. By considering the volume conservation in the recirculation region in (B17) with $U_d s_2$ and the resulting substitution into (B8*a*,*b*), it can be found that the value of D and therefore $\hat{c}$ is not influenced.

Second, we consider the case where the detrainment velocity U_d is not equal to the entrainment velocity U_e, i.e. $U_d \neq U_s$, over the length s_2. By investigating the behaviour of the shear layer we find that $\hat{c}_r$ can be found to be dependent on U_d and by consequence s_2. A brief numerical estimate (not included here) shows that a 10 % increase in $\hat{s}_2$ produces a 6 % change in $\hat{c}_r$. However, from PIV results (see figure 5), we can see that we do not expect a large variation of $\hat{s}_2$, with $\hat{s}_2$ being close to the value of $\hat{s}_1$. Additionally, given the first-order nature of this model, it was felt that this offers an acceptable level of uncertainty for the expected uncertainty in $\hat{s}_2$.

Acknowledgements. The authors would like to thank J. Olsthoorn for reviewing a draft of this paper and the members of staff of the Engineering Department for the help with experimental set-up and maintenance.

Supplementary movies. Supplementary movies are available at https://doi.org/10.1017/flo.2023.14. Raw data are available from the corresponding author (S.C.).

Funding statement. The authors gratefully acknowledge funding by the EPSRC under grant numbers EP/N509620/1 and EP/R513180/1.

Declaration of interests. The authors declare no conflict of interest.

Author contributions. S.C. and M.D.W. created the research plan, designed experiments and formulated the analytical problem. S.C. led model development, performed the experiments and wrote the manuscript with M.D.W. providing providing edits, comments and feedback.

https://doi.org/10.1017/flo.2023.14 Published online by Cambridge University Press

References

Abu-Mulaweh, H., Armaly, B., & Chen, T. (1993). Measurements in buoyancy-assisting laminar boundary layer flow over a vertical backward-facing step - uniform wall heat flux case. *Experimental Thermal and Fluid Science*, *7*(1), 39–48.

Adams, E., & Johnston, J. (1988). Effects of the separating shear layer on the reattachment flow structure part 2: Reattachment length and wall shear stress. *Experiments in Fluids*, *6*(7), 493–499.

Allgayer, D.M., & Hunt, G.R. (2012). On the application of the light-attenuation technique as a tool for non-intrusive buoyancy measurements. *Experimental Thermal and Fluid Science*, *38*, 257–261.

Armaly, B.F., Durst, F., Pereira, J.C.F., & Schönung, B. (1983). Experimental and theoretical investigation of backward-facing step flow. *Journal of Fluid Mechanics*, *127*, 473–496.

Barlow, J., Pope, A., & Rae, W. (1999). *Low-speed wind tunnel testing*. 3rd ed. Wiley.

Brederode, V., & Bradshaw, P. (1973). *Three-dimensional flow in nominally two-dimensional separation bubbles: Flow behind a rearward-facing step. I., Volume 1*. (Thesis, Imperial College of Science and Technology, London, UK).

Caton, F., Britter, R., & Dalziel, S. (2003). Dispersion mechanisms in a street canyon. *Atmospheric Environment*, *37*, 693–702.

Chen, L., Asai, K., Nonomura, T., Guannan, X., & Liu, T. (2018). A review of backward-facing step (BFS) flow mechanisms, heat transfer and control. *Thermal Science and Engineering Progress*, *6*, 194–216.

Essel, E., & Tachie, M. (2015). Roughness effects on turbulent flow downstream of a backward facing step. *Flow Turbulence Combust*, *94*, 125–153.

Hall, S., Behnia, M., Fletcher, C., & Morrison, G. (2003). Investigation of the secondary corner vortex in a benchmark turbulent backward-facing step using cross-correlation particle imaging velocimetry. *Experiments in Fluids*, *35*, 139–151.

Iwai, H., Nakabe, K., Suzuki, K., & Matsubara, K. (1999). Numerical simulation of buoyancy-assisting, backward-facing step flow and heat transfer in a rectangular duct. *Heat Transfer–Asian Research*, *28*(1), 58–76.

Kaye, N., & Linden, P. (2004). Coalescing axisymmetric turbulent plumes. *Journal of Fluid Mechanics*, *502*, 41–63.

Lin, C., Ooka, R., Kikumoto, H., Sato, T., & Arai, M. (2020). Wind tunnel experiment on high-buoyancy gas dispersion around isolated cubic building. *Journal of Wind Engineering and Industrial Aerodynamics*, *202*, 104226.

Mishriky, F., & Walsh, P. (2016). Effect of the backward-facing step location on the aerodynamics of a morphing wing. *MDPI Aerospace*, *3*(3), 25.

Nadge, P., & Govardhan, R. (2014). High reynolds number flow over a backward-facing step: Structure of the mean separation bubble. *Experiments in Fluids*, *55*(1), 1657.

Niemann, M., & Fröhlich, J. (2016). Buoyancy-affected backward-facing step flow with heat transfer at low Prandtl number. *International Journal of Heat and Mass Transfer*, *101*(1), 1237–1250.

Olvera, H., Choudhuri, A., & Li, W. (2008). Effects of plume buoyancy and momentum on the near-wake flow structure and dispersion behind an idealized building. *Journal of Wind Engineering and Industrial Aerodynamics*, *96*, 209–228.

Papadopoulos, G., & Otugen, M. (1995). Separating and reattaching flow structure in a suddenly expanding rectangular duct. *Journal of Fluids Engineering*, *117*(17), 17–23.

Parker, D., Burridge, H., Partridge, J., & Linden, P. (2020). A comparison of entrainment in turbulent line plumes adjacent to and distant from a vertical wall. *Journal of Fluid Mechanics*, *882*, A4.

Rajaratnam, N. (1976). *Turbulent jets*. Elsevier.

Robins, A., & Apsley, D. (2018). Modelling of build effects in ADMS. http://www.cerc.co.uk.

Simoens, S., Ayrault, M., & Wallace, J. (2007). The flow across a street canyon of variable width–part 1: Kinematic description. *Atmospheric Environment*, *41*(39), 9002–9017.

Thielicke, W., & Sonntag, R. (2021). Particle image velocimetry for MATLAB: Accuracy and enhanced algorithms in PIVlab. *Journal of Open Research Software*, *4*, 12.

Tihon, J., Pěnkavovà, V., Havlica, J., & Šimčik, M. (2012). The transitional backward-facing step flow in a water channel with variable expansion geometry. *Experimental Thermal and Fluid Science*, *40*(1), 112–125.

Tominaga, Y., & Stathopoulos, T. (2018). CFD simulations of near-field pollutant dispersion with different plume buoyancies. *Building and Environment*, *131*, 128–139.

Turner, J.S. (1973). *Buoyancy effects in fluids*. Cambridge, UK: Cambridge University Press.

Cite this article: Charlwood S, Frank D, Davies Wykes M (2023). The influence of buoyancy upon pollution trapping and dispersal in the wake of a backward-facing step. *Flow*, *3*, E21. doi:10.1017/flo.2023.14

https://doi.org/10.1017/flo.2023.14 Published online by Cambridge University Press